Journal of Alloys and Compounds 509 (2011) 3690–3698

Contents lists available at ScienceDirect

Journal of Alloys and Compounds

journal homepage: www.elsevier.com/locate/jallcom

$LiFePO_4$/C composite cathode material with a continuous porous carbon network for high power lithium-ion battery

Min Yang[a], Qiuming Gao[a,b,*]

[a] State Key Laboratory of High Performance Ceramics and Superfine Microstructures, Shanghai Institute of Ceramics, Chinese Academy of Sciences, 1295 Dingxi Road, Shanghai 200050, PR China
[b] School of Chemistry and Environment, Beihang University, 37 Xueyuan Road, Beijing 100191, PR China

ARTICLE INFO

Article history:
Received 8 July 2010
Received in revised form
21 December 2010
Accepted 22 December 2010
Available online 30 December 2010

Keywords:
Lithium iron phosphate
Porous carbon network
Cathode material
Power capability
Lithium-ion battery

ABSTRACT

A series of $LiFePO_4$/porous carbon composites with different $LiFePO_4$ loading amounts were prepared by impregnation from ethanol solution of the $LiFePO_4$ precursors. The samples were characterized using X-ray powder diffraction (XRD), thermogravimetry (TG), differential scanning calorimetric (DSC), transmission electron microscopy (TEM) and nitrogen sorption prior to the electrochemical testing. The size and morphology of the porous carbon supported $LiFePO_4$ nanoparticles depended strongly on the $LiFePO_4$ loading amounts. The impact of $LiFePO_4$ loading on the electrochemical performance of the composites was discussed in detail. Among all the samples, the $LiFePO_4$/microporous carbon composites with the $LiFePO_4$ loading amount of 19.10 wt.% and 35.58 wt.%, respectively, demonstrated high rate performance with discharge capacity of 60 mAh g^{-1} and 66 mAh g^{-1} at 50 C.

1. Introduction

In recent years, lithium-ion battery has captured a large share of the rechargeable battery market for its great potential to be used as power sources for electric vehicles (EVs) and hybrid electric vehicles (HEVs) [1,2]. Since the pioneering report by Padhi et al., olivine based lithium iron phosphate has attracted attention attributed to its overwhelming advantages, such as high theoretical capacity of 170 mAh g^{-1}, redox potential of 3.5 V versus Li/Li^+ located in the electrochemical stability window of common non-aqueous electrolytes, low cost, natural abundance and environmental protection [3–8]. However, its large-sized appliance is hampered by its poor performance at high rates as it is a poor conductor of both electrons and Li^+ ions [9–12]. At room temperature, the electronic conductivity of pristine $LiFePO_4$ is only 10^{-9}–10^{-10} S cm^{-1} because the polyanions with strong P–O covalence in $LiFePO_4$ separate the FeO_6 octahedra and dramatically reduce the electronic conductivity of the material [13,14]. Besides, Li^+ ion motion in the olivine crystal structure occurs through one-dimensional channels, which are susceptible to blockage by defects and impurities [15–17]. Considerable efforts in improving the rate capability of $LiFePO_4$ have focused on strategies as follows: (1) improving the electronic and lithium ionic conductivity by doping aliovalent cations on the Li^+ or Fe^{2+} sites [18–20], (2) enhancing the electronic conductivity by carbon coating or conductive polymer coating [21–23], and (3) reducing the diffusion distance of Li^+ by preparing nanosized $LiFePO_4$ materials [24–26].

Nanoparticles with controllable and uniform size supported on carbon are interesting materials for a wide range of applications, such as catalysis, fuel cell, hydrogen storage and supercapacitor [27–30]. The unique properties associated with these materials are due to the specific concentration, size and distribution of the nanoparticles within their host environments [31]. Carbon support is often used attributed to its high surface area and chemical inertness, especially in strong basic and acid environments [32]. In this work, the disordered microporous carbon AC-K5 synthesized by KOH activation of activated carbon in mass ratio of 1:5 [33], and the ordered mesoporous carbon CMK-3 [34] prepared by using ordered mesoporous silica molecular sieve SBA-15 as the template and sucrose as the carbon source, were used as the supports for $LiFePO_4$ nanoparticles, respectively. Since CMK-3 is exactly an inverse replica of SBA-15, the characters of CMK-3 can be tailored depending on the synthetic condition of SBA-15 [35,36]. In order to obtain shorter mesochannels favorable for mass transfer, the hydrothermal temperature of SBA-15 was raised to 160 °C, abbreviated as SBA-15-160. Instead of the solid-state or solution synthesis of $LiFePO_4$ nanoparticles coated with carbon [37,38,15],

---

* Corresponding author at: State Key Laboratory of High Performance Ceramics and Superfine Microstructures, Shanghai Institute of Ceramics, Chinese Academy of Sciences, 1295 Dingxi Road, Shanghai 200050, PR China. Tel.: +86 21 52412513; fax: +86 21 52413122.
E-mail addresses: qmgao@sic.ac.cn, qmgao@buaa.edu.cn (Q. Gao).

0925-8388/$ – see front matter © 2010 Elsevier B.V. All rights reserved.
doi:10.1016/j.jallcom.2010.12.167

where carbon may not cover the entire $LiFePO_4$ surface leading to a discontinuous and hence insufficient conductive network [39,40], the $LiFePO_4$/C composites with a continuous porous carbon network were prepared here. The impact of $LiFePO_4$ loading on the electrochemical performance of $LiFePO_4$/C composites was studied systematically. This study is dedicated to building an energy storage system, which can keep the advantages of both high rate capability and large capacity.

2. Experimental

2.1. Preparation of AC-K5

The AC-K5 was synthesized through KOH activation of activated carbon according to the literature [33]. The mixture of the activated carbon (AC, Shanghai Dahe Chemical Reagent Ltd., chemically pure) and KOH in mass ratio of 1:5, was heated to 750 °C with a heating rate of 1.25 °C min^{-1} under argon. After another 1 h at 750 °C, the obtained product was washed with 3 M hydrochloric acid and deionized water before dried at 100 °C for 12 h.

2.2. Preparation of SBA-15-160 and CMK-3-160

The SBA-15-160 was prepared [41,42] by dissolving 4.0 g of Pluronic P123 triblock copolymer in the mixture of 130 mL of deionized water and 20 mL of concentrated HCl (35 wt.%) with stirring at 35 °C, followed by adding 8.5 g of TEOS. The mixture was stirred at 35 °C for 20 h, and then transferred to an autoclave for further reaction at 160 °C for 48 h. The solid product was filtered, washed with deionized water, dried at 60 °C overnight and finally calcined in air at 550 °C for 6 h to remove the P123 template.

In a typical synthesis of CMK-3-160 (160 denotes the hydrothermal temperature of SBA-15 template) [34,42], 1.0 g of the SBA-15-160 was impregnated with aqueous solution obtained by dissolving 1.3 g of sucrose and 0.14 g of H_2SO_4 in 5.0 g of deionized water. The mixture was then dried at 100 °C for 6 h, and at 160 °C for another 6 h. The resulted powder was treated again at 100 °C and 160 °C for 6 h, respectively, after the addition of 0.8 g of sucrose, 0.09 g of H_2SO_4 and 5.0 g of deionized water. The carbonization was completed by heating at 900 °C for 6 h under nitrogen. The silica template was dissolved with 5 wt.% hydrofluoric acid at room temperature. The template-free carbon thus obtained was filtered, washed with deionized water and ethanol, and dried at 100 °C overnight.

2.3. Synthesis of the $LiFePO_4$/C composites

The $LiFePO_4$/AC-K5 composites with different $LiFePO_4$ loading amounts of theoretical 20 wt.%, 36.9 wt.%, and 60 wt.% abbreviated as LFP/CA-1, 2 and 3, respectively, were prepared by using AC-K5 as the support. Each sample was synthesized with stoichiometric amounts of $Fe(NO_3)_3{\cdot}9H_2O$ (Sinopharm Chemical Reagent Co., Ltd., 98.5%), $LiC_2H_3O_2{\cdot}2H_2O$ (Shanghai Fine Chemical Co., Ltd., Shun Feng, 99.0%) and H_3PO_4 (Sinopharm Chemical Reagent Co., Ltd., 85.0%). In a typical synthesis of LFP/CA-3, 5.9 g of $Fe(NO_3)_3{\cdot}9H_2O$, 1.5 g of $LiC_2H_3O_2{\cdot}2H_2O$, and 1.6 g of H_3PO_4 were dissolved in 20 mL of ethanol with stirring. Then, the transparent solution was incorporated into 2.5 g of AC-K5, followed by drying at 90 °C with stirring. The resulted powder was impregnated again using the solution of 3.9 g of $Fe(NO_3)_3{\cdot}9H_2O$, 1.0 g of $LiC_2H_3O_2{\cdot}2H_2O$ and 1.1 g of H_3PO_4 dissolved in 20 mL of ethanol, followed by drying at 90 °C with stirring prior to calcination. The powder was heated to 300 °C at 2 °C min^{-1} and held at 300 °C for 5 h, before heated at the same rate to 700 °C and held at 700 °C for another 5 h. The calcination was performed under a reductive atmosphere (95% Ar, 5% H_2) to ensure that Fe^{3+} ions were completely reduced to Fe^{2+} ions, and the product was left under the reductive atmosphere until it cooled to room temperature. For preparing the $LiFePO_4$/CMK-3-160 composites with different $LiFePO_4$ loading amount of theoretical 36.9 wt.%, 50 wt.%, and 60 wt.% abbreviated as LFP/CC-1, 2 and 3, respectively, the similar experiments were performed except for using CMK-3-160 as the support.

2.4. Characterization

The structure of the samples was evaluated by X-ray powder diffraction (XRD) recorded on a Rigaku D/MAX-2250 V diffractometer using Cu Ka radiation (40 kV and 40 mA). Transmission electron microscopy (TEM) images and high-resolution transmission electron microscopy (HRTEM) images were taken on a JEOL (JEM-2010) microscope at an accelerating voltage of 200 kV, which equipped with selected area electron diffraction (SAED) and OXFORD Links ISIS energy-dispersive X-ray (EDX) analyses system. The samples were ultrasonic dispersed in ethanol, deposited and dried on a holey carbon film on a copper grid prior to analysis. Nitrogen adsorption–desorption isotherms at 77 K were performed on a Micromeritics Tristar 3000 instrument. Before measurement, all the samples were dried at 150 °C for 12 h under nitrogen. The specific surface area and pore volume were calculated by the Brunauer–Emmett–Teller (BET) and Barrett–Joyner–Halenda (BJH) method, respectively [42]. The carbon content of the $LiFePO_4$/C composites was revealed by the thermogravimetry (TG) and differential scanning calorimetric (DSC) analyses on a STA-409PC/4/H Luxx simultaneous TG-DTA-DSC apparatus (Netzsch, Germany) between 30 °C and 950 °C with a heating rate of 10 °C min^{-1} in air.

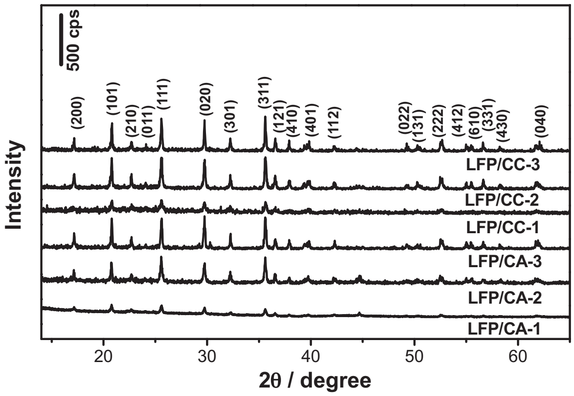

Fig. 1. XRD patterns of the $LiFePO_4$/C composites with different carbon supports and contents.

2.5. Electrochemical analysis

The homogeneous cathode slurry was prepared by milling a mixture of active material, carbon black (Alfa Aesar), poly (vinylidene fluoride) (PVDF, Alfa Aesar) in the weight ratio of 7.5:1.5:1.0 in *N*-methyl-2-pyrrolidone (NMP, Sinopharm Chemical Reagent Co., Ltd.) solvent using a mortar and pestle, before coated onto the Al foil collector. After the solvent evaporation, the electrodes were punched into disks coated with a thin film of 14 mm in diameter and 0.12 mm in thickness, and then dried at 60 °C for 12 h under vacuum. CR2032 coin cells were assembled in an argon-filled glove box for electrochemical testing, which were composed of a lithium foil as the anode, 1 M $LiPF_6$ dissolved in a 1:1 (v/v) mixture of ethylene carbonate (EC) and diethyl carbonate (DEC) as the electrolytes, Celgard polypropylene separator and the prepared cathode sheet. Charge/discharge testing of the cells was undertaken in a potential range of 2.5–4.2 V using a LAND 2001 CT battery test system.

3. Results and discussion

3.1. Structure and composition

As the XRD patterns of $LiFePO_4$/C composites shown in Fig. 1, each sample can be assigned to olivine $LiFePO_4$ with orthorhombic lattice (*P*nma) and there are no detected impurity phases. The intensity of the diffraction peaks gradually increases along with the increased $LiFePO_4$ loading amount. The observed unconspicuous broad wave bands with 2θ between 15° and 35° for LFP/CA-1 and LFP/CC-1 are due to the presence of large amounts of amorphous carbon. A reflection peak typical for the (1 0 0) plane can be observed in the small-angle XRD pattern of CMK-3-160 support (see the supporting information, Fig. S1), indicating the ordered two-dimensional hexagonal (*P*6mm) mesostructure [34]. However, no evident peaks can be found in the small-angle XRD patterns of LFP/CC samples (not shown in Fig. 1), indicating that most of the ordered structure was destroyed in the loading process [43].

The carbon content of $LiFePO_4$/C composites was revealed by the TG and DSC analyses. In the TG curve of LFP/CA-3 (Fig. 2a), the weight loss takes place in three steps appearing at 35–150 °C, 200–320 °C and 320–630 °C with a total weight loss of 42.0%. The first one occurs from 35 °C to around 150 °C, attributed to the evaporation of H_2O. The other steps take place from 200 °C, including both the weight loss due to the carbon oxidation and the weight gain due to the Fe^{2+} oxidation. As the especially large surface area and well developed porous structure of AC-K5 [33] and the catalysis of Fe facilitate the oxidation of carbon, the temperature of the carbon oxidation starts lower than usual. The weight loss at 200–320 °C is most likely due to the partial oxidation of carbon, which further oxidizes at 320–630 °C. In accordance with the TG data, there are one endothermic and two exothermic peaks appearing in the DSC curves correspondingly, indicating the evaporation

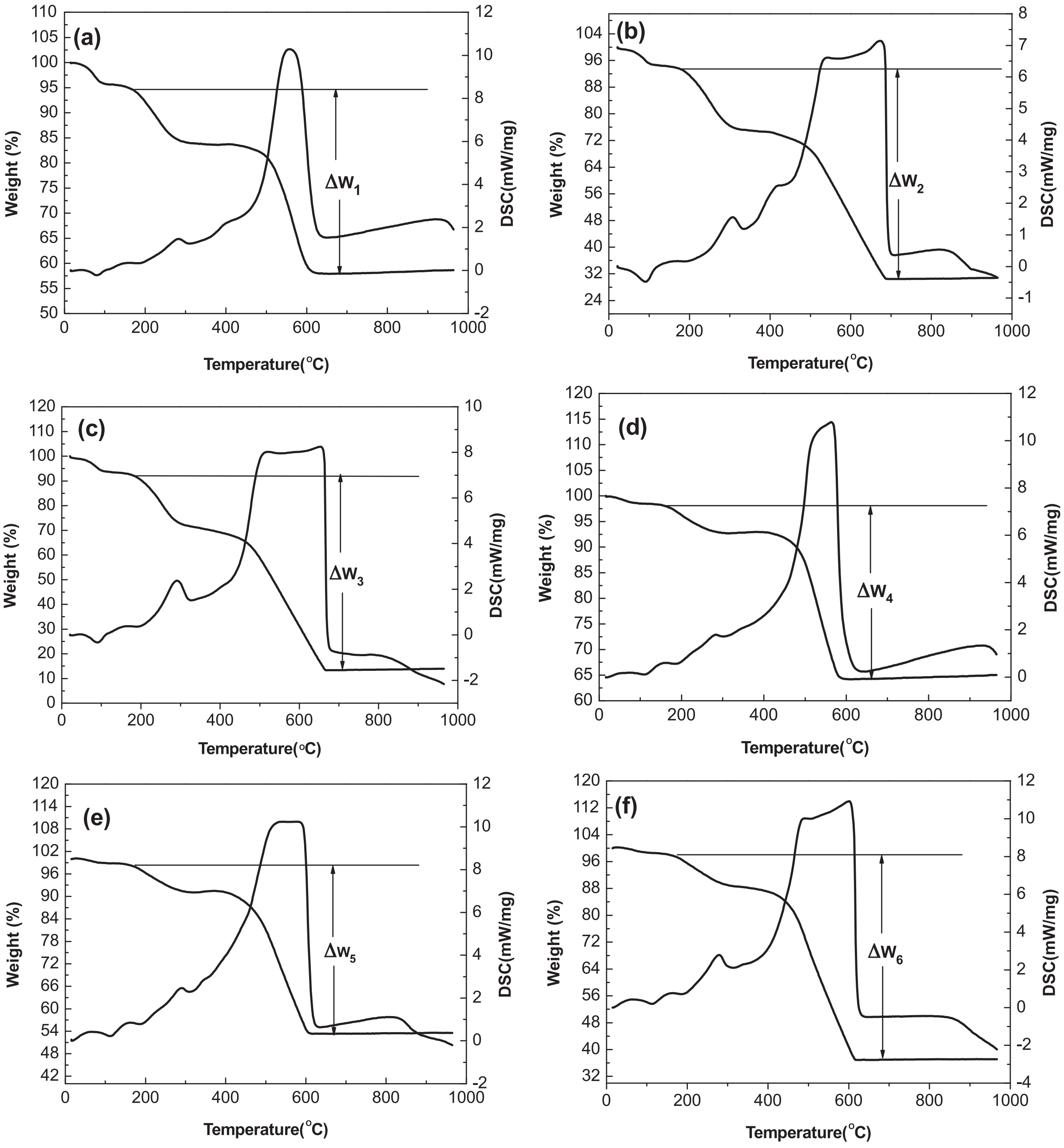

Fig. 2. TG and DSC curves of (a) LFP/CA-3, (b) LFP/CA-2, (c) LFP/CA-1, (d) LFP/CC-3, (e) LFP/CC-2, and (f) LFP/CC-1.

Table 1
Textural properties of the $LiFePO_4$/C composites with different carbon supports and contents.

Samples	S_{BET}[a] ($m^2\ g^{-1}$)	Pore sizes[b] (nm)	Pore volumes[c] ($cm^3\ g^{-1}$)	Theoretical carbon contents (wt.%)	Carbon contents[d] (wt.%)
AC-K5	2894	2.44	1.46	100	–
LFP/CA-1	1397	2.65	0.70	80.0	80.90
LFP/CA-2	1282	2.66	0.64	63.1	64.42
LFP/CA-3	708	2.76	0.35	40.0	39.07
CMK-3-160	714	6.15	0.92	100	–
LFP/CC-1	572	5.87	0.65	63.1	63.56
LFP/CC-2	424	6.00	0.49	50.0	47.99
LFP/CC-3	356	6.00	0.40	40.0	37.13

[a] Surface areas calculated by the Brunauer–Emmett–Teller (BET) method.

[b] BJH desorption average pore diameters (4V/A).

[c] Total pore volumes measured at $p/p_0 = 0.97$.

[d] The weight contents of carbon estimated from thermogravimetry (TG) analyses.

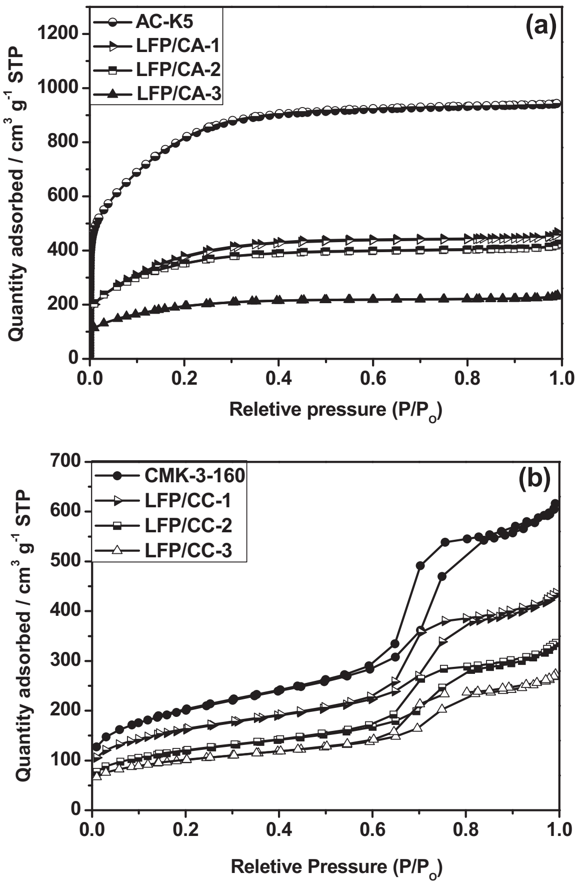

Fig. 3. Nitrogen adsorption–desorption isotherms of (a) AC-K5 and LFP/CA composites and (b) CMK-3-160 and LFP/CC composites.

of H_2O and stepwise oxidation of carbon. It should be mentioned that in the temperature range of 230–530 °C, the oxidation of Fe^{2+} ions took place ($12LiFePO_4 + 3O_2 \rightarrow 4Li_3Fe_2(PO_4)_3 + 2Fe_2O_3$) and the theoretical weight gain of 5.07% for the sample should be observed [44,45]. However, since the weight gain during the oxidation of $LiFePO_4$ was much less than the weight loss in the oxidation of carbon, both the TG and DSC features for the oxidation of $LiFePO_4$ were heavily screened by the strong exothermic oxidation bands of carbon appearing as a small shoulder at 380–450 °C. For the same reason, the TG and DSC behaviors of other samples shown in Fig. 2 are similar. The actual carbon content can be calculated from the TG data [44] and the results are summarized in Table 1.

3.2. *Textural properties and morphology*

The nitrogen adsorption–desorption isotherms of AC-K5 and LFP/CA composites shown in Fig. 3a are mixed types I and IV with well-defined plateaus, indicating the apparent micropore character. The nitrogen sorption isotherms of CMK-3-160 and LFP/CC composites shown in Fig. 3b are type IV according to the IUPAC classification and exhibit a H1 hysteresis loop typical for mesoporous structure. As listed in Table 1, the BET surface area and pore volume of LFP/CA and LFP/CC composites systematically decrease with increased $LiFePO_4$ content, respectively. The variation in the pore size of LFP/CC composites affirms that most of the $LiFePO_4$ particles grew on the surface of CMK-3-160 with increased $LiFePO_4$ loading amount. Compared with the LFP/CC composites, it is worth mentioning that the surface areas of LFP/CA composites are much larger due to the presence of AC-K5 support with especially large surface area, which is attributed to the well developed micropore structure of AC-K5.

TEM images shown in Fig. 4a and b for LFP/CA-1 reveals a good dispersion of sphere-like $LiFePO_4$ nanoparticles (10–50 nm) on the AC-K5 support. AC-K5 formed a framework to bind $LiFePO_4$ particles together and provided a hindrance to the growth and aggregation of crystalline. As AC-K5 is a microporous carbon into which the ions of precursor hardly immerge, the especially large surface area of AC-K5 plays a dominating role in forming uniform $LiFePO_4$ nanoparticles on the support. However, the morphology control effect of AC-K5 weakens with increased $LiFePO_4$ content. Large and irregular $LiFePO_4$ particles are more frequently observed in Fig. 4c–f, reflecting the influence that heavier $LiFePO_4$ loading leading to a higher degree of the growth and aggregation of crystalline with a wider size distribution of 20–300 nm for LFP/CA-2 and 20–800 nm for LFP/CA-3, respectively. The $LiFePO_4$ nanoparticles in LFP/CA-3 were further investigated by HRTEM and SAED. A highly crystalline character with a distinct lattice spacing of 0.511 nm corresponding to the (0 2 0) plane is observed in the HRTEM image (Fig. 4g). The single crystal nature and the relevant XRD results of $LiFePO_4$ particles are obviously supported by the SAED pattern (Fig. 4h). For LFP/CC-1, well dispersed sphere-like $LiFePO_4$ nanoparticles (15–70 nm) were incorporated with CMK-3-160 (Fig. 5a), as the confinement effect of the mesochannels in CMK-3-160 acted when the $LiFePO_4$ precursor condensed. However, further increasing the content of $LiFePO_4$, more aggregates are found as shown in Fig. 5b and c. Similarly, the confinement effect of CMK-3-160 on crystal growth and aggregation weakens with increased $LiFePO_4$ loading amount.

3.3. *Charge/discharge behaviors*

The typical charge/discharge processes of AC-K5 and LFP/CA composites in 2.5–4.2 V at 0.2 C are shown in Fig. 6a and b, and the result of each LFP/CA composite was based on the whole composite, containing both the $LiFePO_4$ and carbon. It is obvious that four cells showed different electrochemical behaviors. As shown in Fig. 6a, the discharge capacity of AC-K5 is 32.2 mAh g^{-1} attributed to the interfacial anion adsorbing/desorbing process. The discharge capacity increased to 68 mAh g^{-1} for LFP/CA-1 after AC-K5 loaded with 19.10 wt.% $LiFePO_4$, which shows two modes of energy storage resulting in slope of the charge/discharge plateau [46,47]. The discharge capacity shown in Fig. 6b is 92.2 mAh g^{-1} for LFP/CA-2 and 122.5 mAh g^{-1} for LFP/CA-3, respectively, with much flatter and longer discharge plateaus compared with that of LFP/CA-1, indicating that more $LiFePO_4$ component brought charge storage ability into act. As to CMK-3-160 and LFP/CC composites, the typical charge/discharge processes in 2.5–4.2 V at 0.2 C are shown in Fig. 6c and d, and the result of each LFP/CC composite was based on the whole composite, containing both the $LiFePO_4$ and carbon. As shown in Fig. 6c, the discharge capacity of CMK-3-160 was 52.9 mAh g^{-1}, attributed to the interfacial anion adsorbing/desorbing process. The discharge capacity of LFP/CC-1 was 87.6 mAh g^{-1}, with a capacity enhancement of 66% compared with that of CMK-3-160. The discharge capacity and the capacity enhancement compared with that of CMK-3-160 are 114.4 mAh g^{-1} and 116% for LFP/CC-2, and 93.7 mAh g^{-1} and 77% for LFP/CC-3, respectively (Fig. 6d). The capacity enhancement is caused by the introduction of $LiFePO_4$ with high capacity. Based on the results, it can be deduced that the whole charge/discharge processes of both LFP/CA and LFP/CC composites include not only the extraction/insertion of Li^+ ions in $LiFePO_4$, but also the electric double-layer electrostatic adsorbing/desorbing of PF_6^- in porous carbon, combining both the faradic energy storage and electric double-layer energy

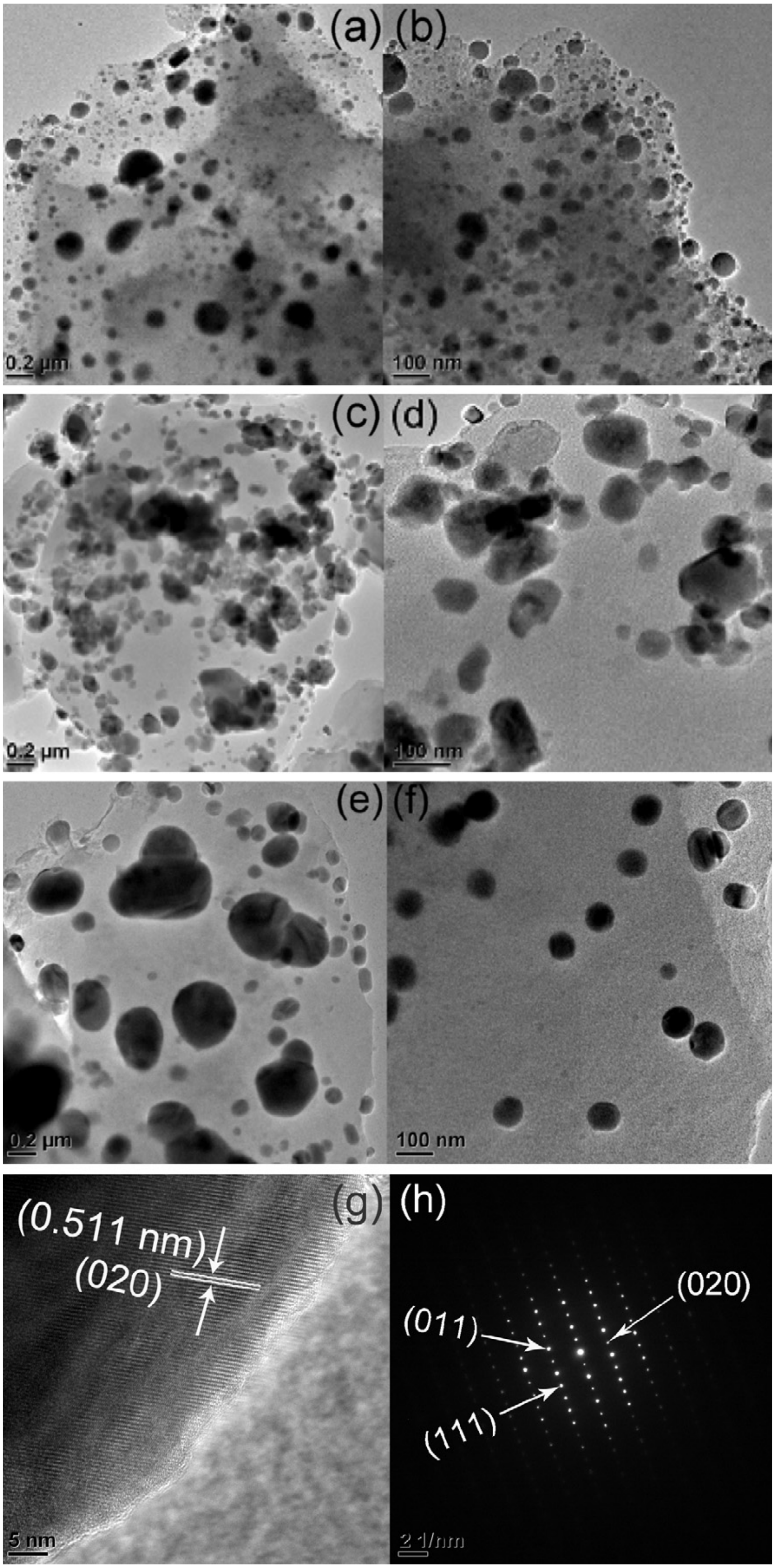

Fig. 4. TEM images of (a and b) LFP/CA-1, (c and d) LFP/CA-2, and (e,and f) LFP/CA-3. And (g) HRTEM image and (h) SAED pattern of the $LiFePO_4$ particle in LFP/CA-3.

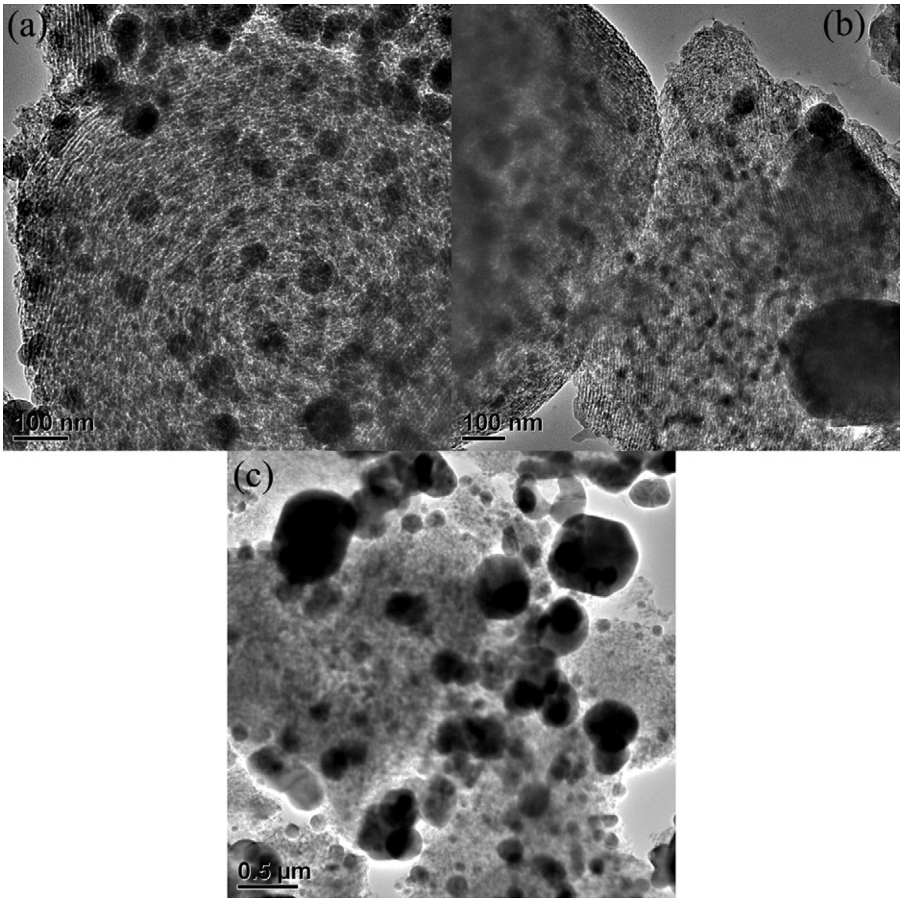

Fig. 5. TEM images of (a) LFP/CC-1, (b) LFP/CC-2, and (c) LFP/CC-3.

storage. It is noteworthy that LFP/CA-2 reached higher capacity than LFP/CC-1, and LFP/CA-3 reached higher capacity than LFP/CC-3, respectively, though the capacity of AC-K5 support was much lower than that of the CMK-3-160 support. As the carbon contents of the compared pair were similar, it is indicated that large surface area can enhance the capacity of electrode material due to the sufficient interaction between electrode and electrolyte.

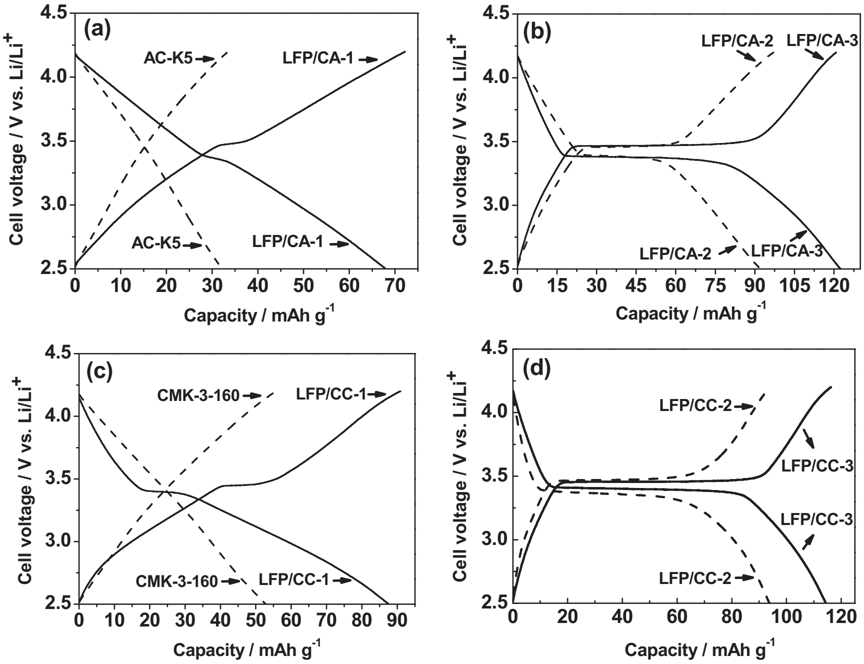

Fig. 6. Typical charge/discharge curves of (a) AC-K5 and LFP/CA-1, (b) LFP/CA-2 and 3, (c) CMK-3-160 and LFP/CC-1, and (d) LFP/CC-2 and 3 at 0.2 C.

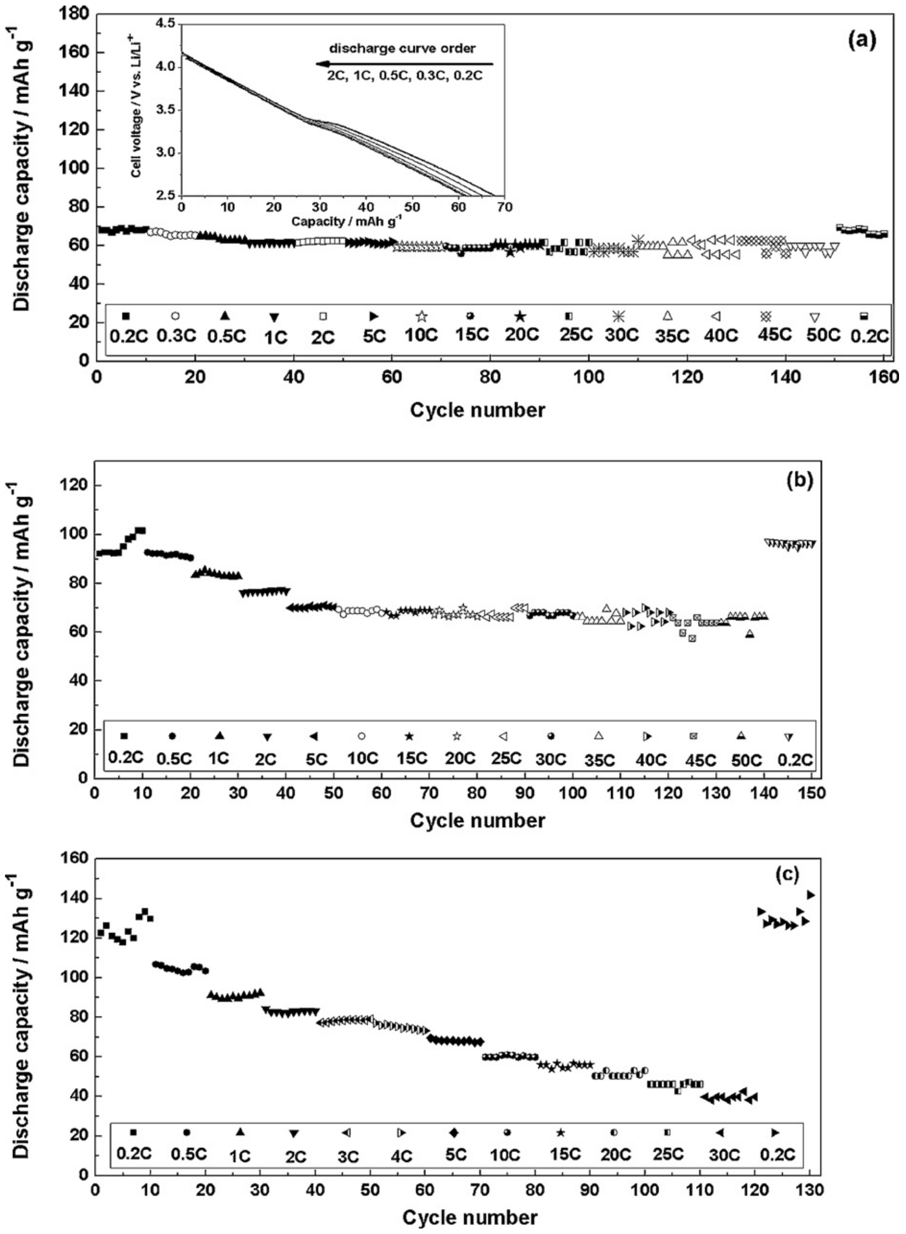

Fig. 7. Cycling performance of (a) LFP/CA-1, (b) LFP/CA-2 at different rates from 0.2 C to 50 C and finally back to 0.2 C, and (c) LFP/CA-3 from 0.2 C to 30 C and finally back to 0.2 C. The inset in (a) is typical discharge curves of LFP/CA-1 at different rates from 0.2 C to 2 C, and the order of the discharge curves is as shown by the arrow.

3.4. Cycling and rate performance

The LFP/CA batteries were cycled ten times at each rate from 0.2 C to 50 C to determine the available capacity for each sample and finally cycled at 0.2 C again to ensure that the electrode had completely recovered from the cycling at high rates. Each result was based on the whole composite, containing both the $LiFePO_4$ and carbon. For LFP/CA-1, as shown in the inset of Fig. 7a, the discharge curves at different rates are characterized by three distinct features commonly seen in the literatures of $LiFePO_4$ electrodes, namely (1) a flatter plateau at low rate due to the coexistence of two phases during discharge; (2) a decrease in the plateau potential with increased current rate; and (3) an increased slope in the plateau region with increased current rates. It indicates a drop in the utilization of $LiFePO_4$ through two-phase redox reaction between $LiFePO_4$ and $FePO_4$ with increased current rates. The fluctuation and fading of capacity became more serious after 30 C (Fig. 7a). The following reasons are inferred. First, SEI film partially breaks up and repairs by itself at high rates due to the change of the structure of material, leading to increased polarization and uncertain consumption of Li^+. Second, resistance at the interface between the material and current collector may cause heat generation, especially at high current rates, leading to fluctuation and fading of capacity since the electrochemical performance of battery is sensitive to temperature. The discharge capacity of LFP/CA-1 in the tenth cycle of 50 C is 60 mAh g^{-1}, corresponding to the capacity retention of 88%, compared with the value of 68 mAh g^{-1} in the tenth cycle of 0.2 C. The excellent capacity retention is attributed to the following reasons: (1) the charge transfer is efficient as AC-K5 maintains a continuous and conductive network; (2) the reducing particle size distributed in 10–50 nm and the homogeneous sphere-like morphology improve the lithium-ion transition rate by decreasing the diffusion distance; and (3) both the interaction between electrode and electrolyte and the adsorption of Li^+ from electrolyte are facilitated by the large surface area of LFP/CA-1 and the porous structure of AC-K5 support. The discharge capacity of LFP/CA-2 in the tenth

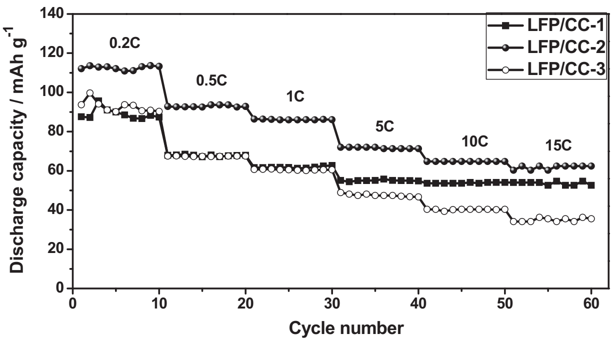

Fig. 8. Comparison of the cycling performance of LFP/CC composites at different rates from 0.2 C to 15 C.

cycle of 0.2 C and 50 C was 101 and 66 mAh g^{-1} (Fig. 7b), respectively, corresponding to the capacity retention of 65%. The discharge capacity of LFP/CA-3 in the tenth cycle of 0.2 C and 30 C was 130 and 40 mAh g^{-1} (Fig. 7c), respectively, corresponding to the capacity retention of only 31%. The capacity retention of LFP/CA composites obviously decreased as the $LiFePO_4$ loading amount increased, caused by the large size of $LiFePO_4$ particles together with the evidently decreased surface area. Full recovery of the capacity with slightly higher value was observed in all the LFP/CA samples when the current rate returned to 0.2 C after hundreds of cycles, indicating their excellent cycling stability. The LFP/CC batteries were cycled ten times at each rate from 0.2 C to 15 C to determine the available capacity for each sample as shown in Fig. 8. Compared with the discharge capacity at 0.2 C in the tenth cycle, the capacity retention at 15 C in the sixtieth cycle is 60% for LFP/CC-1, 55% for LFP/CC-2 and 39% for LFP/CC-3, respectively. The capacity retention of LFP/CC composites decreased as the $LiFePO_4$ loading amount increased, illustrating the same trend with the LFP/CA composites due to the above reason.

There has been some similar research work before, such as $LiFePO_4$/AC composite with the $LiFePO_4$ content of 21.1 wt.% showed a capacity of 40.08 mAh g^{-1} at 4 C [47], which was much lower than the value achieved by LFP/CA-1; and $LiFePO_4$/carbon monolith sample with the carbon content of 68% reached 100 mAh g^{-1} at 0.1 C [46], which was comparable to the value achieved by LFP/CA-2. The enhancement of large carbon content on the rate performance of $LiFe_{0.9}P_{0.95}O_{4-\delta}$ has been researched by Kang and Ceder before [17]. However, unlike Kang's work, in which the 65 wt.% carbon black was added as an electric additive in preparing the tested electrode, the material presented in this work inherently featured a continuous porous carbon network over which $LiFePO_4$ nanoparticles loaded offering structural connection. The concept of combination of two modes of energy storage such as supercapacitor and battery may have a significant impact on the rate performance of lithium-ion battery.

4. Conclusions

Well dispersed $LiFePO_4$ nanoparticles combining the disordered microporous carbon AC-K5 and ordered mesoporous cabon CMK-3-160 as a support, respectively, were prepared by impregnation. The size, morphology and dispersibility of the resultant $LiFePO_4$ nanoparticles were observed with great dependence on the $LiFePO_4$ loading amount. Lower loading amount of $LiFePO_4$ resulted in more homogeneous dispersion of particles with narrower size distribution. Among all the samples, LFP/CA-1 and LFP/CA-2 demonstrated preferable rate capability with discharge capacity at 50 C of 60 mAh g^{-1} and 66 mAh g^{-1}, respectively. The material is potentially ideal at high rate attributed to the structure of small $LiFePO_4$ nanoparticles supported on a continuous porous carbon network with high surface area, through which both the transition of Li^+ ions and electrons improves. Though the work presented here may not be suitable for the real application of battery now due to the large contents of carbon, the related research on new material design combining both the high rate capability of supercapacitor and large capacity of battery thus blurring the traditional distinction between them is thought to be meaningful.

Acknowledgements

This work was financially supported by the National Basic Research Program of China (973 Program, No. 2011CB935700), Chinese National Science Foundation (No. U0734002) and Shanghai Basic Key Program (No. 09JC1415100).

Appendix A. Supplementary data

Supplementary data associated with this article can be found, in the online version, at doi:10.1016/j.jallcom.2010.12.167.

References

[1] N. Hua, C.Y. Wang, X.Y. Kang, T. Wumair, Y. Han, J. Alloys Compd. 503 (2010) 204–208.
[2] Y.S. Hu, Y.G. Guo, R. Dominko, M. Gaberscek, J. Jamnik, J. Maier, Adv. Mater. 19 (2007) 1963–1966.
[3] A.K. Padhi, K.S. Nanjundaswamy, J.B. Goodenough, J. Electrochem. Soc. 144 (1997) 1188–1194.
[4] S.B. Lee, I.C. Jang, H.H. Lim, V. Aravindan, H.S. Kim, Y.S. Lee, J. Alloys Compd. 491 (2010) 668–672.
[5] H. Liu, G.X. Wang, D. Wexler, J.Z. Wang, H.K. Liu, Electrochem. Commun. 10 (2008) 165–169.
[6] Y. Cui, X.L. Zhao, R.S. Guo, Electrochim. Acta 55 (2010) 922–926.
[7] T. Muraliganth, A.V. Murugan, A. Manthiram, J. Mater. Chem. 18 (2008) 5661–5668.
[8] C.M. Doherty, R.A. Caruso, B.M. Smarsly, C.J. Drummond, Chem. Mater. 21 (2009) 2895–2903.
[9] J. Xu, G. Chen, Physica B 405 (2010) 803–807.
[10] K. Saravanan, M.V. Reddy, P. Balaya, H. Gong, B.V.R. Chowdari, J.J. Vittal, J. Mater. Chem. 19 (2009) 605–610.
[11] Y.G. Wang, Y.R. Wang, E.J. Hosono, K.X. Wang, H.S. Zhou, Angew. Chem. Int. Ed. 47 (2008) 7461–7465.
[12] J.K. Kim, J.W. Choi, G.S. Chauhan, J.H. Ahn, G.C. Hwang, J.B. Choi, H.J. Ahn, Electrochim. Acta 53 (2008) 8258–8264.
[13] Y.F. Wang, D. Zhang, X. Yu, R. Cai, Z.P. Shao, X.Z. Liao, Z.F. Ma, J. Alloys Compd. 492 (2010) 675–680.
[14] A.V. Murugan, T. Muraliganth, A. Manthiram, Electrochem. Commun. 10 (2008) 903–906.
[15] D. Jugovic, D. Uskokovic, J. Power Sources 190 (2009) 538–544.
[16] S. Nishimura, G. Kobayashi, K. Ohoyama, R. Kanno, M. Yashima, A. Yamada, Nat. Mater. 7 (2008) 707–711.
[17] B. Kang, G. Ceder, Nature 458 (2009) 190–193.
[18] G.R. Gardiner, M.S. Islam, Chem. Mater. 22 (2010) 1242–1248.
[19] L. Wu, X.H. Li, Z.X. Wang, X.J. Wang, L.J. Li, J. Fang, F.X. Wu, H.J. Guo, Powder Technol. 199 (2010) 293–297.
[20] Z.R. Chang, H.J. Lv, H.W. Tang, X.Z. Yuan, H.J. Wang, J. Alloys Compd. 501 (2010) 14–17.
[21] L.Q. Sun, M.J. Li, R.H. Cui, H.M. Xie, R.S. Wang, J. Phys. Chem. C 114 (2010) 3297–3303.
[22] A. Fedorkova, A.N. Alejos, P.G. Romero, R. Orinakova, D. Kaniansky, Electrochim. Acta 55 (2010) 943–947.
[23] Y. Zhang, H. Feng, X.B. Wu, L.Z. Wang, A.Q. Zhang, T.C. Xia, H.C. Dong, M.H. Liu, Electrochim. Acta 54 (2009) 3206–3210.
[24] R. Yang, X.P. Song, M.S. Zhao, F. Wang, J. Alloys Compd. 468 (2009) 365–369.
[25] H. Uchiyama, H. Imai, Cryst. Growth Des. 10 (2010) 1777–1781.
[26] K. Saravanan, P. Balaya, M.V. Reddy, B.V.R. Chowdari, J.J. Vittal, Energy Environ. Sci. 3 (2010) 457–464.
[27] Y. Takasu, T. Kawaguchi, W. Sugimoto, Y. Murakami, Electrochim. Acta 48 (2003) 3861–3868.
[28] H.T. Kim, H.I. Joh, S.H. Moon, J. Power Sources 195 (2010) 1352–1358.
[29] H.S. Kim, H. Lee, K.S. Han, J.H. Kim, M.S. Song, M.S. Park, J.Y. Lee, J.K. Kang, J. Phys. Chem. B 109 (2005) 8983–8986.
[30] G.M. Jacob, Q.M. Yang, I. Zhitomirsky, J. Appl. Electrochem. 39 (2009) 2579–2585.
[31] K.S. Morley, P.C. Marr, P.B. Webb, A.R. Berry, F.J. Allison, G. Moldovan, P.D. Brown, S.M. Howdle, J. Mater. Chem. 12 (2002) 1898–1905.
[32] Q.H. Tang, Y.T. Chen, Y.H. Yang, J. Mol. Catal. A: Chem. 315 (2010) 43–50.
[33] H.L. Wang, Q.M. Gao, J. Hu, J. Am. Chem. Soc. 131 (2009) 7016–7022.

[34] S. Jun, S.H. Joo, R. Ryoo, M. Kruk, M. Jaroniec, Z. Liu, T. Ohsuna, O. Terasaki, J. Am. Chem. Soc. 122 (2000) 10712–10713.
[35] A. Vinu, M. Hartmann, Catal. Today 102 (2005) 189–196.
[36] A.B. Fuertes, Micropor. Mesopor. Mater. 67 (2004) 273–281.
[37] V. Drozd, G.Q. Liu, R.S. Liu, H.T. Kuo, C.H. Shen, D.S. Shy, X.K. Xing, J. Alloys Compd. 487 (2009) 58–63.
[38] A.V. Murugan, T. Muraliganth, A. Manthiram, J. Phys. Chem. C 112 (2008) 14665–14671.
[39] H.M. Xie, R.S. Wang, J.R. Ying, L.Y. Zhang, A.F. Jalbout, H.Y. Yu, G.L. Yang, X.M. Pan, Z.M. Su, Adv. Mater. 18 (2006) 2609–2613.
[40] X.L. Wu, L.Y. Jiang, F.F. Cao, Y.G. Guo, L.J. Wan, Adv. Mater. 21 (2009) 2710–2714.
[41] D.Y. Zhao, J.L. Feng, Q.S. Huo, N. Melosh, G.H. Fredrickson, B.F. Chmelka, G.D. Stucky, Science 279 (1998) 548–552.
[42] K.S. Xia, Q.M. Gao, C.D. Wu, S.Q. Song, M.L. Ruan, Carbon 45 (2007) 1989–1996.
[43] H.J. Zhang, H.H. Tao, Y. Jiang, Z. Jiao, M.H. Wu, B. Zhao, J. Power Sources 195 (2010) 2950–2955.
[44] Y.L. Cao, L.H. Yu, T. Li, X.P. Ai, H.X. Yang, J. Power Sources 172 (2007) 913–918.
[45] V. Palomares, A. Goni, L.G. de Muro, I. de Meatza, M. Bengoechea, O. Miguel, T. Rojo, J. Power Sources 171 (2007) 879–885.
[46] C.M. Doherty, R.A. Caruso, B.M. Smarsly, P. Adelhelm, C.J. Drummond, Chem. Mater. 21 (2009) 5300–5306.
[47] X. Hu, Y. Huai, Z. Lin, J. Suo, Z. Deng, J. Electrochem. Soc. 154 (2007) A1026–A1030.